



# Binder-Free Charantia-Like Metal-Oxide Core/Shell Nanotube Arrays for High-Performance Lithium-Ion Anodes

Pingping Xu<sup>1</sup>, Ziyang Zhang<sup>1\*</sup>, Huizhen Zhang<sup>2</sup>, Ao Shen<sup>1</sup>, Yangqiang Zhao<sup>1</sup>, Yangyang Zhou<sup>1</sup> and Ying Weng<sup>1</sup>

<sup>1</sup> School of Materials Engineering, Shanghai University of Engineering Science, Shanghai, China, <sup>2</sup> School of Management, University of Shanghai for Science and Technology, Shanghai, China

## OPEN ACCESS

### Edited by:

James Rohan,  
University College Cork, Ireland

### Reviewed by:

Maksudul Hasan,  
Newcastle University, United Kingdom  
Xinhui Xia,  
Zhejiang University, China

### \*Correspondence:

Ziyang Zhang  
zzying@sues.edu.cn

### Specialty section:

This article was submitted to  
Electrochemistry,  
a section of the journal  
Frontiers in Chemistry

Received: 03 December 2019

Accepted: 21 February 2020

Published: 06 March 2020

### Citation:

Xu P, Zhang Z, Zhang H, Shen A,  
Zhao Y, Zhou Y and Weng Y (2020)  
Binder-Free Charantia-Like  
Metal-Oxide Core/Shell Nanotube  
Arrays for High-Performance  
Lithium-Ion Anodes.  
Front. Chem. 8:159.  
doi: 10.3389/fchem.2020.00159

The performance of anodes of lithium-ion batteries relies largely on the architecture and composition of the hybrid active materials. We present a two-step, seed-free, solution-based method for the direct growth of hierarchical charantia-like TiO<sub>2</sub>/Fe<sub>2</sub>O<sub>3</sub> core/shell nanotube arrays on carbon cloth substrates. An ultrahigh loading of the nanomaterial on carbon fibers was achieved with this method without the use of a binder. This three-dimensional porous hollow architecture and its direct contact with the CC current collector ensure an efficient electronic pathway. The hollow TiO<sub>2</sub> framework effectively protects the hierarchical charantia-like TiO<sub>2</sub>/Fe<sub>2</sub>O<sub>3</sub> hollow core/shell arrays from collapsing because of its negligible volume change during cycling. Meanwhile, the self-assembled  $\alpha$ -Fe<sub>2</sub>O<sub>3</sub> hollow nanospheres guarantee a large capacity and contact area with the electrolyte. This flexible anode with a 3D porous charantia-like hollow architecture exhibits high cycle performance, reversible capacity, and rate capability. These nanotube arrays maintain a high reversible capacity of 875 mAh g<sup>-1</sup> after 200 cycles at a current density of 200 mA g<sup>-1</sup>. This simple, cost-effective, and scalable electrode fabrication strategy can be implemented in the fabrication of high-performance wearable energy storage devices.

**Keywords:** carbon fabric, TiO<sub>2</sub> nanotube arrays,  $\alpha$ -Fe<sub>2</sub>O<sub>3</sub> hollow nanospheres, lithium-ion batteries, anodes

## INTRODUCTION

Lithium-ion batteries (LIBs) are popular energy storage devices because of their high energy density, high open-circuit voltage, lack of memory effects, and shape controllability (Joshi et al., 2016; Zhao et al., 2016; Shen et al., 2018; Deng et al., 2019). The design of electrode materials with high energy density and cycling stability is important for enhancing the performance of LIBs. Graphite—the most widely used commercial anode material—cannot fulfill the increasing demands with regard to the energy density and stability of an electrode owing to its low theoretical capacity (372 mAh g<sup>-1</sup>), poor rate performance, and intrinsic stability. Therefore, much attention has been focused on exploring anode materials with higher capacity for next-generation LIBs (Liu et al., 2019; Partheeban and Sasidharan, 2019; Shen et al., 2019).

TiO<sub>2</sub> is a promising anode candidate owing to its relatively good conductivity, low cost, higher operation voltage, and low volume expansion. However, its practical application is impeded by its

low theoretical capacity. Owing to its unique physical and chemical properties as a nanomaterial, TiO<sub>2</sub> is engineered into various nanostructures with different morphologies to improve the specific capacity (Moretti et al., 2013; Ying et al., 2017; Smith et al., 2019). Despite immense progress in this area, the effect of scaling down on the performance of TiO<sub>2</sub> has been limited due to its theoretical capacity limitation. Recent studies have indicated that TiO<sub>2</sub>-based nanocomposites obtained by combining them with high-capacity metal oxides could facilitate high performance at a smaller scale (Zhu et al., 2014; Wang et al., 2015; Lee et al., 2017; Yang et al., 2018; Zhang et al., 2019). Hematite ( $\alpha$ -Fe<sub>2</sub>O<sub>3</sub>) is a promising mineral for preparing a hybrid with TiO<sub>2</sub> because of its relatively higher theoretical capacity ( $\sim 1,000 \text{ mA h g}^{-1}$ ), non-toxicity, high corrosion resistance, and abundant resource (Gao et al., 2014; Li et al., 2016; Jiang et al., 2017; Zhao et al., 2019). When Fe<sub>2</sub>O<sub>3</sub> is anchored onto the surface of a TiO<sub>2</sub> nano-backbone, its high theoretical capacity compensates for the deficient capacity of the TiO<sub>2</sub> nano-backbone, while the good conductivity and low volume expansion of TiO<sub>2</sub> ensures excellent cyclic stability of the hybrid material (Luo et al., 2012; Yang et al., 2017). One-dimensional (1D) nanotube arrays and three-dimensional (3D) hollow spheres can promote rate capability by offering an efficient electronic pathway (Han et al., 2011; Wang et al., 2012; He et al., 2018). Therefore, we fabricated 3D nanotube arrays by coating Fe<sub>2</sub>O<sub>3</sub> hollow nanospheres on TiO<sub>2</sub> nanotube arrays to realize high-performance rechargeable batteries. However, the direct growth of a 3D porous hollow composite architecture on a flexible substrate without a binder remains a major challenge.

In this study, 3D hierarchical charantia-like TiO<sub>2</sub>/Fe<sub>2</sub>O<sub>3</sub> nanotube arrays were grown directly on a carbon cloth (CC) substrate by a facile hydrothermal method. The CC/TiO<sub>2</sub> nanotube arrays decreased the fracture risk caused by the volume fluctuation during lithium-ion insertion and extraction, while the  $\alpha$ -Fe<sub>2</sub>O<sub>3</sub> nanosphere shell assembled on the surface of TiO<sub>2</sub> nanotube increased the surface area and number of active sites. Direct contact of the active material with the CC substrate and the hollow structure facilitated an efficient electronic pathway. Their unique hollow core-shell structure endowed the final electrodes with high energy, reversible capacity, and cycle performance.

## EXPERIMENTAL METHOD

### Synthesis of TiO<sub>2</sub> Nanotube Arrays on CC

Before the experiment, the CC substrates were immersed in nitric acid at 30°C for 3 h, and then ultrasonically cleaned with distilled water and ethanol for 30 min. TiO<sub>2</sub> nanotube arrays were synthesized by a facile hydrothermal method. Analytically pure reagents were used without further purification. Typically, 1 mL of tetrabutyl titanate, 12 mL of glycerinum, and 45 mL of ethanol were magnetically stirred at room temperature to form a homogeneous precursor solution. The precursor was then poured into a 100 mL Teflon-lined autoclave with a piece of clean CC (7 × 5.0 cm) and maintained at 175°C for 20 h. After the reaction, the white byproduct on the CC was washed with ethanol and distilled water, and CC/TiO<sub>2</sub> nanotube arrays were obtained after heating the products at 350°C for 1 h.

### Growth of Fe<sub>2</sub>O<sub>3</sub> Nanospheres on CC/TiO<sub>2</sub> Nanotube Arrays

The as-prepared CC/TiO<sub>2</sub> nanotube arrays were used as scaffolds for growing  $\alpha$ -Fe<sub>2</sub>O<sub>3</sub> hollow nanospheres via a simple hydrothermal method. FeCl<sub>3</sub>·6H<sub>2</sub>O (1.688 g) and ammonia (0.1 mL) were dissolved in 40 mL of deionized water in a 100 mL Pyrex beaker and stirred to form a clear tan solution. The final mixture was transferred to an 80 mL Teflon-lined autoclave and heated at 95°C for 4 h. The products were washed several times with ethanol and water. The dried products were further annealed in a N<sub>2</sub> atmosphere at 450°C for 2 h.

### Characterization of the Structure and Morphology

Phase purity of the synthesized products was examined by X-ray powder diffraction (XRD, Panalytical X'Pert, Netherlands) carried out with Cu-K $\alpha$  radiation ( $\lambda = 1.5418 \text{ \AA}$ ). The morphology of the products was characterized by field-emission scanning electron microscopy (SEM, Model: JEOL JSM-7000F, Japan) and high-resolution transmission electron microscopy (HRTEM, Model: FEI Titan X 60-300, USA). FA1004 electronic balance was used to measure the weight difference between the prepared electrode and CC substrate, and the mass loading of the active material was obtained. X-ray photoelectron spectroscopy (XPS) was performed on a Perkin-Elmer model PHI 5600 XPS system, with a monochromated aluminum anode as the X-ray source. The specific surface area of the obtained products was calculated by the Brunauer–Emmett–Teller (BET) method using the nitrogen adsorption–desorption isotherm acquired from a Micrometics Tristar 3000 system.

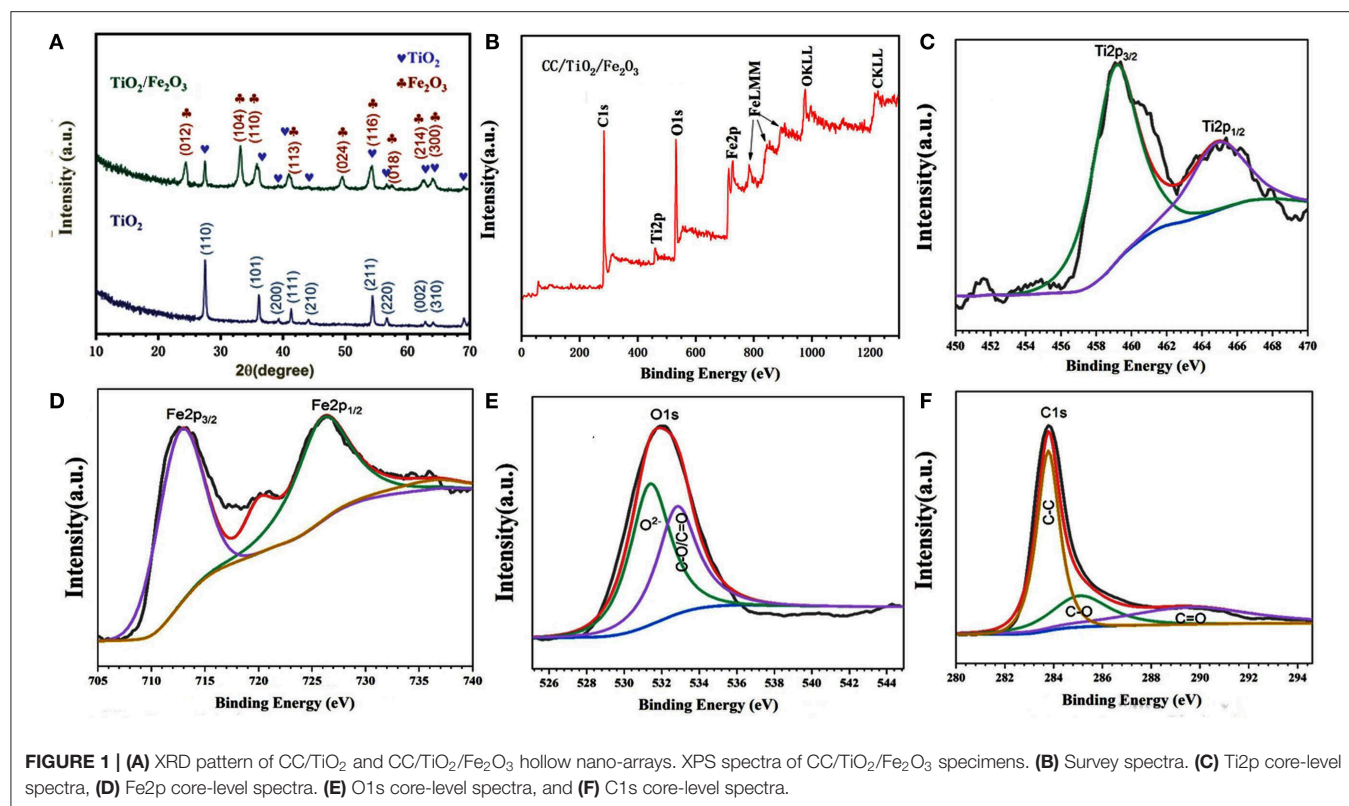
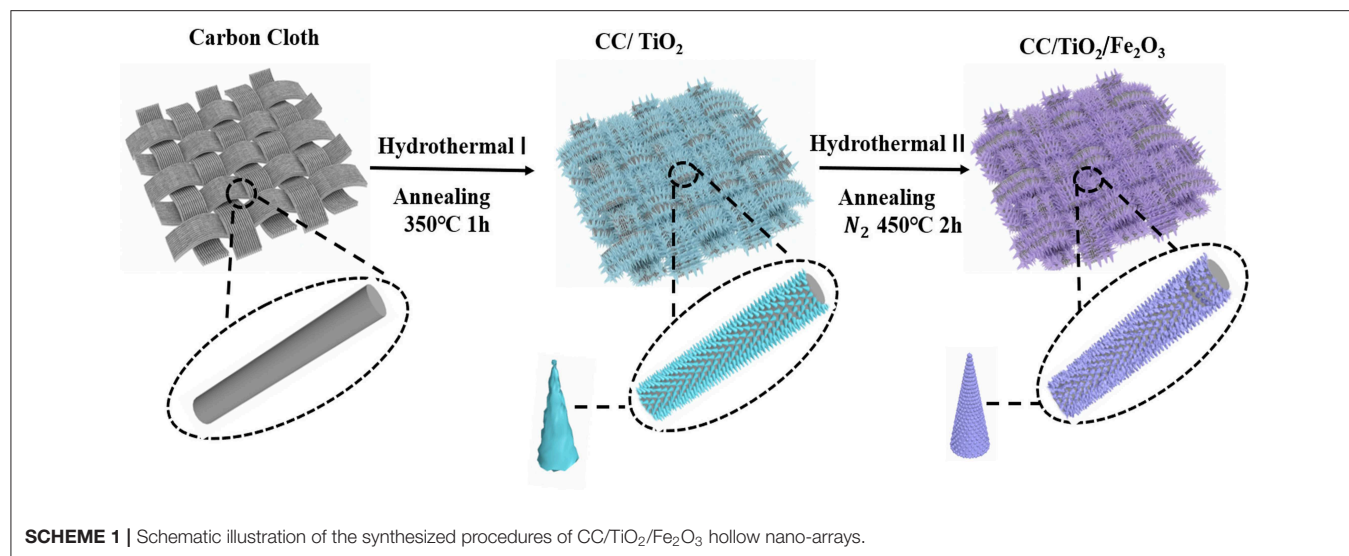
### Electrochemical Measurements

Electrochemical tests were performed in CR 2032 coin half-cells assembled in an argon-filled glovebox using the as-prepared hierarchical nanotube arrays as the anode and circular lithium-metal foil as the cathode. A solution of 1 M LiPF<sub>6</sub> in ethylene carbonate and diethyl carbonate at a volume ratio of 1:1 was used as the electrolyte. The cells were galvanostatically charged and discharged using a multichannel battery tester (Neware-CT3008). With lithium-metal foil as the counter and reference electrodes, Cyclic voltammetry (CV) of the coin half-cells was performed on a PARSTAT 4000 electrochemical workstation at a scan rate of 0.2 mV s<sup>-1</sup> in the range of 3.0–0.01 V vs. Li/Li<sup>+</sup>. Electrochemical impedance spectroscopy (EIS) was performed in a wide frequency range of 100 kHz to 0.01 Hz at an AC perturbation voltage of 5 mV.

## RESULTS AND DISCUSSION

### Synthesis and Characterization

Scheme 1 shows the synthesis of the 3D hierarchical charantia-like CC/TiO<sub>2</sub>/Fe<sub>2</sub>O<sub>3</sub> nanotube arrays. First, the TiO<sub>2</sub> nanotube arrays were fabricated on a CC substrate by a facile seed-free hydrothermal method. After annealing the obtained product in air at 350°C for 1 h, the amorphous TiO<sub>2</sub> cores crystallized into one-dimensional (1D) CC/TiO<sub>2</sub> nanotube arrays. Subsequently, ultrathin FeOOH nanosheets were



grown on the surface of the CC/TiO<sub>2</sub> nanotube arrays and then spontaneously transformed into hollow nanospheres by the forced hydrolysis of FeCl<sub>3</sub>, without the use of any structure-directing agent. FeOOH hollow nanospheres grown on the CC/TiO<sub>2</sub> nanotube arrays were further transformed into  $\alpha$ -Fe<sub>2</sub>O<sub>3</sub> hollow nanospheres through thermal dehydroxylation and lattice shrinkage at a high temperature, leading to the formation of the charantia-like CC/TiO<sub>2</sub>/Fe<sub>2</sub>O<sub>3</sub> nanotube arrays.

XRD measurements were performed to confirm the crystalline structure of the obtained products. **Figure 1A** shows the corresponding XRD patterns of TiO<sub>2</sub> and TiO<sub>2</sub>/Fe<sub>2</sub>O<sub>3</sub> products scratched from CC substrates. All the diffraction peaks of the TiO<sub>2</sub> products matched well with those of typical tetragonal rutile TiO<sub>2</sub> (JCPDS No. 21-1272). The lattice parameters of the obtained tetragonal rutile TiO<sub>2</sub> nanotube are  $a = b = 4.516$  Å and  $c = 5.205$  Å. These are consistent with those reported by Luo et al. (2012). Three additional peaks were observed in

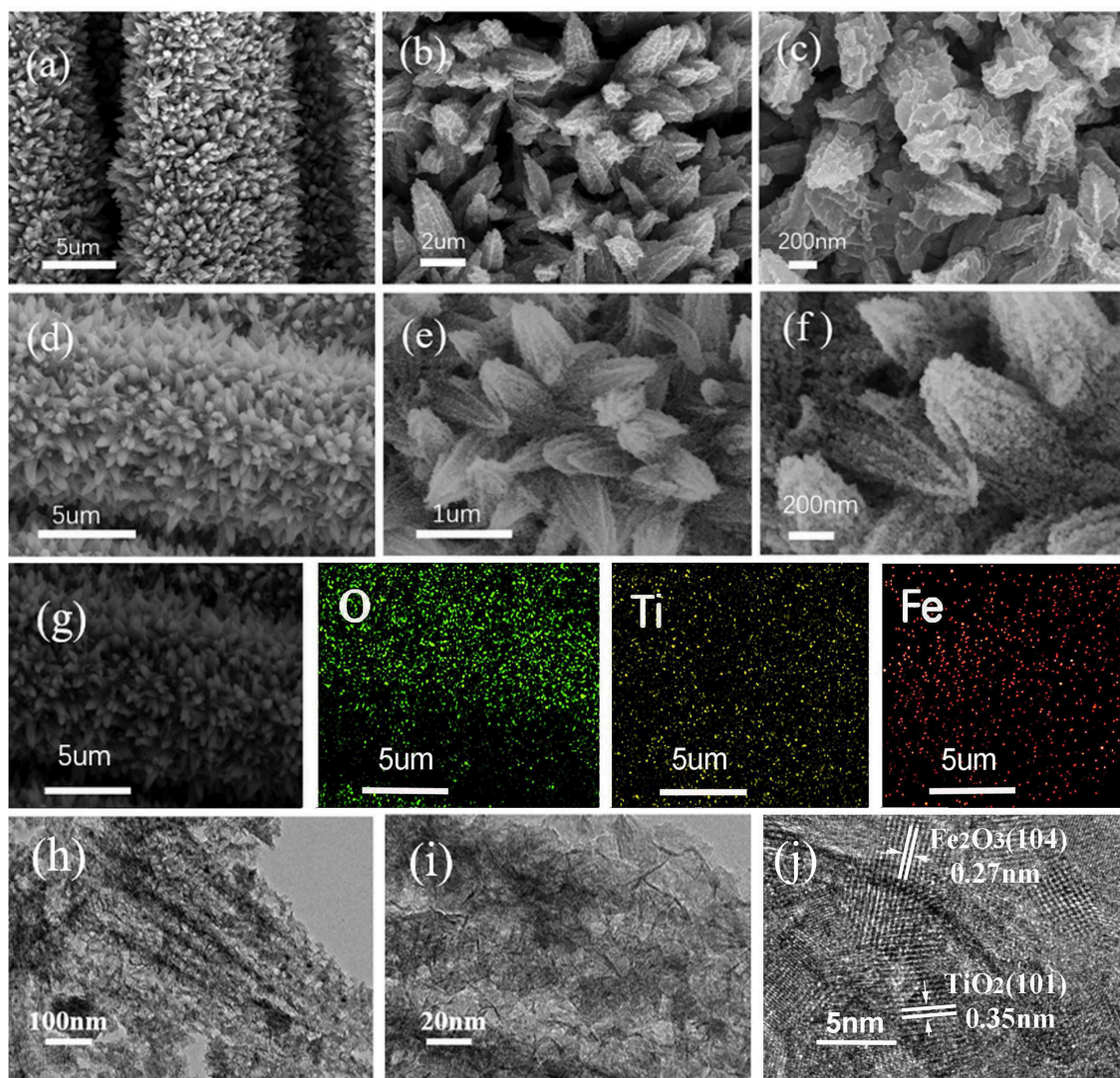


**FIGURE 2** | SEM images of the prepared specimens at different magnifications. (a–c) CC/TiO<sub>2</sub> specimens. (d–f) CC/TiO<sub>2</sub>/Fe<sub>2</sub>O<sub>3</sub> specimens. (g) EDX elemental mapping of the CC/TiO<sub>2</sub>/Fe<sub>2</sub>O<sub>3</sub> specimens. (h–j) TEM and HRTEM images of CC/TiO<sub>2</sub>/Fe<sub>2</sub>O<sub>3</sub> specimens.

the XRD pattern of the TiO<sub>2</sub>/Fe<sub>2</sub>O<sub>3</sub> composite. These peaks located at 33.1, 35.6, and 54.1° correspond to the (104), (110), and (116) planes of  $\alpha$ -Fe<sub>2</sub>O<sub>3</sub> (JCPDS No. 33-0664), respectively, indicating the successful preparation of an  $\alpha$ -Fe<sub>2</sub>O<sub>3</sub> shell on the TiO<sub>2</sub> nanotube core (Larcher et al., 2003; Qi et al., 2018).

XPS was performed to identify the chemical states and surface composition of the final composite. The spectra are shown in **Figures 1B–F**. Only the peaks of Ti, O, Fe, and C are found in the survey spectrum of the CC/TiO<sub>2</sub>/Fe<sub>2</sub>O<sub>3</sub> composite. The XPS spectrum of the C 1s core-level could be divided into three peaks (**Figure 1C**). The peak at 283.7 eV indicates the non-oxygenated carbon. The other two peaks at 284.9 and 289.1 eV correspond to the carbon ramifications generated in the hydrothermal reaction and annealing process. The deconvoluted peaks of the O 1s spectrum could also be decomposed into two

components centered at 531.3 and 533.8 eV, respectively. The low binding energy component is attributed to the O<sub>2</sub><sup>-</sup> attached to Ti and Fe, the other component corresponds to the oxygen in C–O and O–C=O bonds. The Ti 2p XPS spectrum exhibits bimodal characteristics. The peaks located at 460 and 466 eV correspond to Ti 2p<sub>3/2</sub> and Ti 2p<sub>1/2</sub>, respectively (Wang et al., 2016). The binding energy difference of 5.8 eV between the Ti 2p<sub>1/2</sub> and Ti 2p<sub>3/2</sub> core levels indicated that the oxidation state of Ti is mainly Ti (4+). Similarly, the typical bimodal characteristics of the Fe 2p XPS spectrum also confirmed the existence of surface Fe as a trivalent oxide (Luo et al., 2012; Yang et al., 2017). Consistent with the results of XRD, the XPS analysis revealed that the obtained composites are composed of  $\alpha$ -Fe<sub>2</sub>O<sub>3</sub> and TiO<sub>2</sub>.

The morphology and microstructure of the as-obtained composite were characterized by SEM and TEM. **Figures 2a–c**

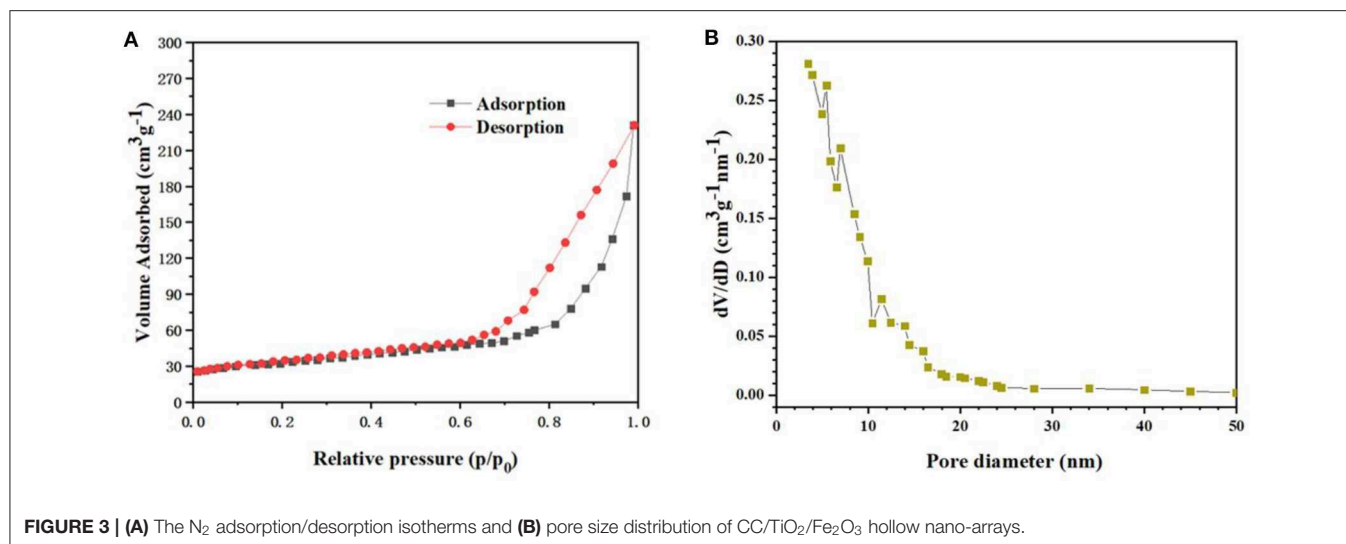


FIGURE 3 | (A) The N<sub>2</sub> adsorption/desorption isotherms and (B) pore size distribution of CC/TiO<sub>2</sub>/Fe<sub>2</sub>O<sub>3</sub> hollow nano-arrays.

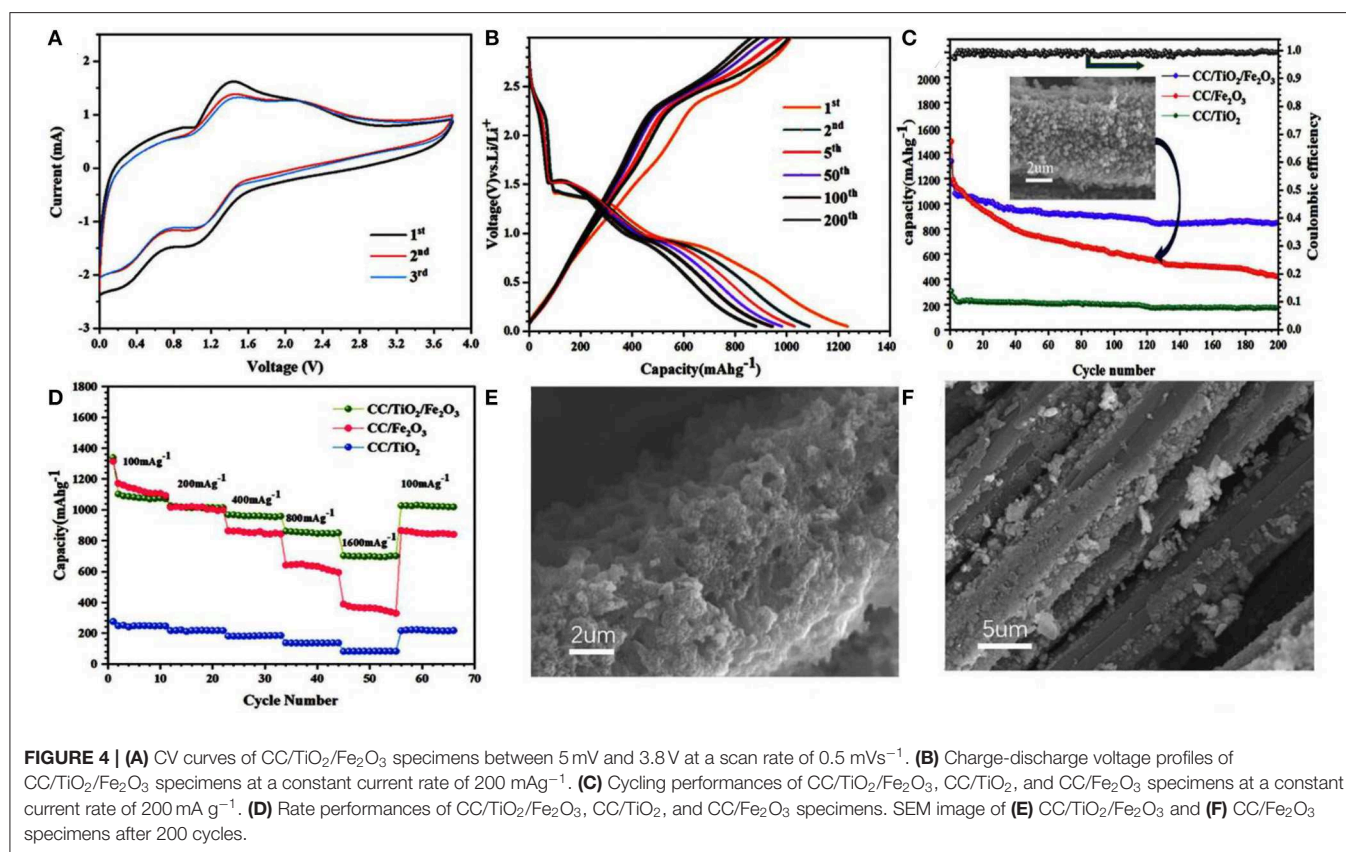


FIGURE 4 | (A) CV curves of CC/TiO<sub>2</sub>/Fe<sub>2</sub>O<sub>3</sub> specimens between 5 mV and 3.8 V at a scan rate of 0.5 mVs<sup>-1</sup>. (B) Charge-discharge voltage profiles of CC/TiO<sub>2</sub>/Fe<sub>2</sub>O<sub>3</sub> specimens at a constant current rate of 200 mA g<sup>-1</sup>. (C) Cycling performances of CC/TiO<sub>2</sub>/Fe<sub>2</sub>O<sub>3</sub>, CC/TiO<sub>2</sub>, and CC/Fe<sub>2</sub>O<sub>3</sub> specimens at a constant current rate of 200 mA g<sup>-1</sup>. (D) Rate performances of CC/TiO<sub>2</sub>/Fe<sub>2</sub>O<sub>3</sub>, CC/TiO<sub>2</sub>, and CC/Fe<sub>2</sub>O<sub>3</sub> specimens. SEM image of (E) CC/TiO<sub>2</sub>/Fe<sub>2</sub>O<sub>3</sub> and (F) CC/Fe<sub>2</sub>O<sub>3</sub> specimens after 200 cycles.

show the SEM images of pure CC/TiO<sub>2</sub> nanotube arrays at different magnifications. It is obvious that the 1D TiO<sub>2</sub> nanotube arrays grew uniformly and vertically on the CC substrate in a carambola-like configuration. The high-magnification SEM images clearly show that the 1D carambola-like TiO<sub>2</sub> nanotube arrays have a mean bottom diameter of 500 nm. Their walls were assembled from several small nanosheets, leading to the roughening of the surface of the TiO<sub>2</sub>

nanotube arrays. A rough surface facilitates the heterogeneous nucleation of Fe<sub>2</sub>O<sub>3</sub> nanoparticles. **Figures 2d–f** present the SEM images of CC/TiO<sub>2</sub>/Fe<sub>2</sub>O<sub>3</sub> nanocomposite arrays at different magnifications. As seen, a large number of nanospheres adhered to the surface of the carambola-like TiO<sub>2</sub> nanotube arrays, forming a 3D hierarchical charantia-like structure. This association rendered the final nanotube arrays more compact and spatially dense, thus guaranteeing a high mass loading and

**TABLE 1** | List of research reports on TiO<sub>2</sub>/Fe<sub>2</sub>O<sub>3</sub> as lithium-ion anodes.

Materials	Capacity/constant current density	Cycles	References
CC/TiO <sub>2</sub> /Fe <sub>2</sub> O <sub>3</sub> nanotube arrays	896 mAh g <sup>-1</sup> , 200 mA g <sup>-1</sup>	200 cycles	This work
TiO <sub>2</sub> @α-Fe <sub>2</sub> O <sub>3</sub> on carbon textiles	480 mAh g <sup>-1</sup> , 120 mA g <sup>-1</sup>	150 cycles	Luo et al., 2012
TiO <sub>2</sub> @α-Fe <sub>2</sub> O <sub>3</sub> carbon coated	516 mAh g <sup>-1</sup> , 200 mA g <sup>-1</sup>	200 cycles	Luo et al., 2013
TiO <sub>2</sub> -B@α-Fe <sub>2</sub> O <sub>3</sub>	785 mAh g <sup>-1</sup> , 100 mA g <sup>-1</sup>	100 cycles	Xia et al., 2014
TiO <sub>2</sub> @α-Fe <sub>2</sub> O <sub>3</sub>	600 mAh g <sup>-1</sup> , 200 mA g <sup>-1</sup>	200 cycles	Luo et al., 2013

high specific capacity. The mass loading of CC/TiO<sub>2</sub>/Fe<sub>2</sub>O<sub>3</sub> nanocomposite arrays was ~11.6 mg cm<sup>-2</sup>, higher than that of the pure TiO<sub>2</sub>/CC nano-arrays (~5.1 mg cm<sup>-2</sup>). Owing to these features, the final nanotube arrays can remain ordered without undergoing any apparent structural collapse or breakage. Compared with the bare TiO<sub>2</sub> nanotube arrays, the bottom diameters of the 3D hierarchical CC/TiO<sub>2</sub>/Fe<sub>2</sub>O<sub>3</sub> nano-composite arrays range up to 700 nm, with negligible variation in the length. The surface of the charantia-like CC/TiO<sub>2</sub>/Fe<sub>2</sub>O<sub>3</sub> nanotube arrays is rougher and looser than that of the 1D bare CC/carambola-like TiO<sub>2</sub> nanotube arrays. These characteristics improved the effective contact area with the electrolyte. Furthermore, the robust bottom of the charantia-like nano-composite arrays increased their mechanical strength, thus reducing the fracture risk triggered by volume variations during lithiation/delithiation. This unique structure may lead to a large specific capacity and high cycling stability of the final product (Joshi et al., 2016; Zhang et al., 2019). **Figure 2g** displays the EDX mapping analysis of the charantia-like CC/TiO<sub>2</sub>/Fe<sub>2</sub>O<sub>3</sub> nanotube arrays. Fe, Ti, and O are evenly distributed on the surface of carbon fibers, further implying that the nanospheres coated on the surface of 1D TiO<sub>2</sub> nanotube arrays are iron oxides.

To investigate the microstructure of the charantia-like nanotube arrays, further TEM observations were made. **Figures 2h–j** show the TEM images of the nanotube arrays scraped off the CC substrate. **Figure 2h** shows that both the TiO<sub>2</sub> cores and Fe<sub>2</sub>O<sub>3</sub> nanospheres have hollow interiors. The hollow Fe<sub>2</sub>O<sub>3</sub> nanospheres are loosely assembled from numerous small nanosheets, indicating that they might have a mesoporous structure. Further, the HRTEM image shows that the lattice spacings of the 3D hierarchical charantia-like CC/TiO<sub>2</sub>/Fe<sub>2</sub>O<sub>3</sub> nanotube arrays are 0.35 and 0.27 nm, corresponding to the (101) plane of tetragonal rutile TiO<sub>2</sub> and the (110) plane of α-Fe<sub>2</sub>O<sub>3</sub>, respectively (Luo et al., 2012; Qi et al., 2018). This result further confirms that the nanotube arrays were composed of tetragonal rutile TiO<sub>2</sub> and α-Fe<sub>2</sub>O<sub>3</sub>.

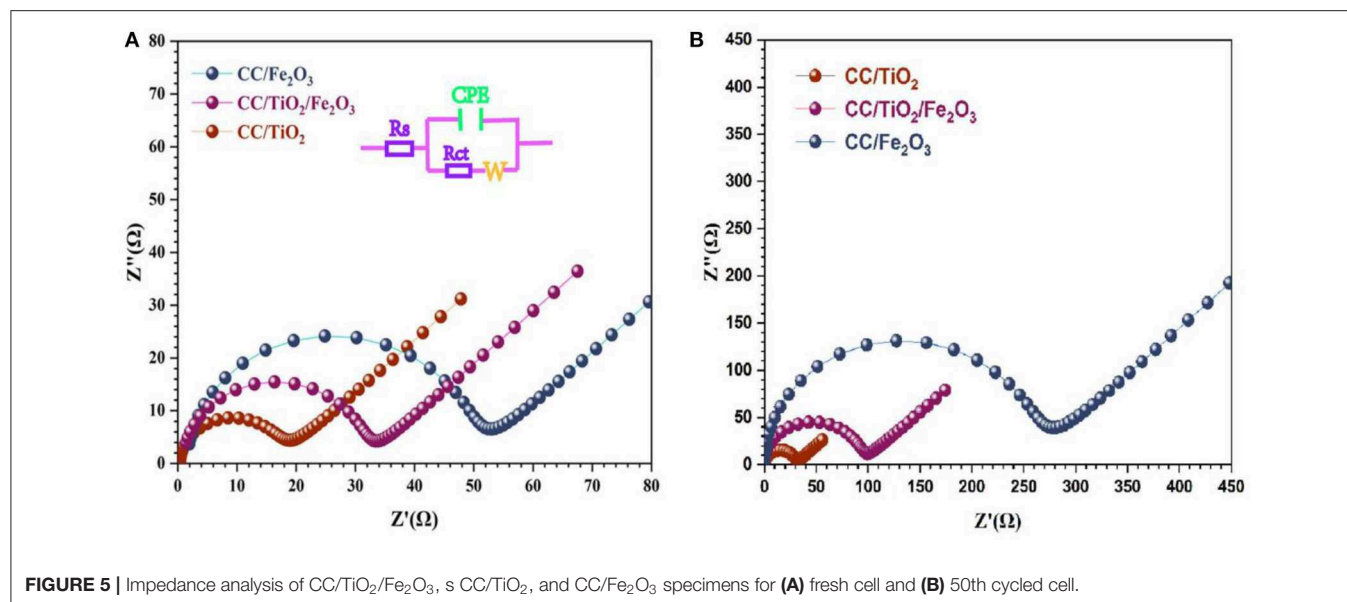
BET gas-sorption measurements were performed to further investigate the porous nature and the specific surface area of the nanotube arrays. **Figure 3A** presents the nitrogen

adsorption–desorption isotherm of the nanotube arrays. The typical IV isotherm with a distinct hysteresis loop in the range of 0.7–1.0 P/P<sub>0</sub> indicates that the charantia-like TiO<sub>2</sub>/Fe<sub>2</sub>O<sub>3</sub> nanotube arrays have a mesoporous structure (Luo et al., 2013; Zhang et al., 2019). The BET specific surface area of the nanotube arrays was calculated to be 149.3 m<sup>2</sup> g<sup>-1</sup>. The large specific surface area is mainly due to the extremely uneven charantia-like surface resulting from the well-wrapped Fe<sub>2</sub>O<sub>3</sub> hollow nanospheres. The pore size distribution (**Figure 3B**) demonstrates that the main pore size of the nanotube arrays is approximately 13.4 nm. According to the literature (Luo et al., 2012; Wang et al., 2016; Zhang et al., 2019), such a mesoporous structure can offer enough interface for lithium-ion insertion and extraction.

## Electrochemical Properties

The electrochemical properties of the 3D hierarchical charantia-like CC/TiO<sub>2</sub>/Fe<sub>2</sub>O<sub>3</sub> nanotube arrays were evaluated to further confirm the performance of the prepared nanotube arrays. **Figure 4A** shows the first three CV cycles of a single redox couple in the voltage window of 0–3.8 V at a scanning rate of 0.5 mV/s. The first CV curve shows two broad cathodic peaks at 1.05 and 0.42 V, which mainly correspond to the generation of Li<sub>2</sub>O as well as the formation of a solid-electrolyte interface (SEI) (Luo et al., 2012; Yang et al., 2017). In the anodic process, the peak at 1.4 V indicates the oxidation of zero-valent iron to ferric iron, while the weak peak at 2.3 V is ascribed to the delithiation of TiO<sub>2</sub>. Except for the slight variation in the two cathodic peaks, the subsequent curves exhibit good reproducibility. The slight shift in the two cathodic peaks to higher potential reveal the occurrence of some irreversible processes during the first cycle. This result is consistent with the previous findings reported in literature (Luo et al., 2012; Qi et al., 2018; Zhang et al., 2019).

**Figure 4B** shows different cycle charge–discharge voltage profiles of the 3D hierarchical charantia-like CC/TiO<sub>2</sub>/Fe<sub>2</sub>O<sub>3</sub> nanotube arrays at a constant current density of 200 mA g<sup>-1</sup>. The plateau voltages in the first discharge curve are in good agreement with the oxidation peaks in the CV curves. The initial discharge and charge capacities are ~1,280 and 1,089 mAh g<sup>-1</sup>, respectively, corresponding to a low irreversible capacity loss (~15%). **Figure 4C** shows the cycling performances of the CC/TiO<sub>2</sub>/Fe<sub>2</sub>O<sub>3</sub> nanotube arrays as along with those of CC/TiO<sub>2</sub> nanotube arrays and CC/Fe<sub>2</sub>O<sub>3</sub> composites. The CC/Fe<sub>2</sub>O<sub>3</sub> composites were synthesized from clean CC using the same Fe ion hydrothermal system mentioned in the experimental section. Although the bare CC/TiO<sub>2</sub> nanotube arrays presented a perfect cycle performance, they had a low capacity. On the contrary, despite having a high capacity in the initial stage, the CC/Fe<sub>2</sub>O<sub>3</sub> composite showed a rapid decay of the capacity with cycling. The apparent decline in the capacity is mainly due to the drastic volume changes of Fe<sub>2</sub>O<sub>3</sub> itself during lithiation, which led to the removal of the active material from the CC substrate. By contrast, the combination of low volume expansion of the TiO<sub>2</sub> hollow cores and the strong adhesion between the two types of metallic oxides rendered the structure of the 3D nanotube arrays stable during lithium-ion insertion/extraction processes. This feature further led to



high cyclic capacity retention of the nanotube arrays. Even after 200 cycles, the discharge capacity of the CC/TiO<sub>2</sub>/Fe<sub>2</sub>O<sub>3</sub> nanotube arrays was maintained at approximately 896 mAh g<sup>-1</sup>, which is much higher than that of the bare CC/TiO<sub>2</sub> nanotube arrays and CC/Fe<sub>2</sub>O<sub>3</sub> composites. At the 200th cycle, the Coulombic efficiency of the nanotube array electrodes was approximately 98.7%. **Figure 4D** displays the rate performance of the tested electrodes in the rate range of 100–1,600 mA g<sup>-1</sup>. The CC/TiO<sub>2</sub>/Fe<sub>2</sub>O<sub>3</sub> nanotube array electrode maintained a discharge capacity of approximately 742 mAh g<sup>-1</sup> even when the discharge rate was increased to 1,600 mA g<sup>-1</sup>. Meanwhile, the discharge capacity of the CC/Fe<sub>2</sub>O<sub>3</sub> composite electrode was only approximately 397.5 mA g<sup>-1</sup> at 1,600 mA g<sup>-1</sup>. Compared the previous literature (Luo et al., 2012, 2013; Xia et al., 2014), these charantia-like nanotube arrays exhibit superior capacity and cyclability due to their unique double hollow structure (**Table 1**).

**Figures 4E,F** illustrate the SEM images of the CC/TiO<sub>2</sub>/Fe<sub>2</sub>O<sub>3</sub> nanotube array and the CC/Fe<sub>2</sub>O<sub>3</sub> composite electrodes after 200 cycles. The former maintained an integral framework and was tightly adsorbed to the surface of the CC substrate after 200 cycles. Under the same condition, the volume of Fe<sub>2</sub>O<sub>3</sub> itself changed unprecedentedly upon cycling, resulting in a large alternate stress. As a result, the CC/Fe<sub>2</sub>O<sub>3</sub> composite severely fragmented and extensively separated from the CC substrate. Consistent with the charge-discharge test results, the electrical contact loss significantly reduced the cycling life of the CC/Fe<sub>2</sub>O<sub>3</sub> composite electrode.

To gain further insight into the electrochemical performance of the test specimens, EIS measurements were carried out at room temperature. **Figures 5A,B** show the Nyquist plots of the test specimens at their open-circuit voltage. All the test specimens exhibited semi-circular Nyquist plots in the high-frequency region and a straight line in the low-frequency region.

The diameter of the semicircle represents the charge-transfer resistance ( $R_{CT}$ ), while the slope of the line corresponds to the mass transfer of lithium ions ( $W$ ) (Shen et al., 2019; Zhang et al., 2019). By adding the Ohmic resistance ( $R_s$ ) and double-layer capacitance ( $CPE$ ), the electrochemical system can be fitted to the Randles circuit shown in **Figure 5A**. As shown in **Figure 5**, the diameters of the semicircle of the 3D hierarchical charantia-like CC/TiO<sub>2</sub>/Fe<sub>2</sub>O<sub>3</sub> nanotube arrays and bare CC/TiO<sub>2</sub> nano-arrays are smaller than that of the CC/Fe<sub>2</sub>O<sub>3</sub> composite, indicating that the conductivity of the hollow CC/TiO<sub>2</sub>/Fe<sub>2</sub>O<sub>3</sub> nano-arrays can be effectively improved by their TiO<sub>2</sub> nanotube cores. After 200 cycles, the charge-transfer resistance of the CC/TiO<sub>2</sub>/Fe<sub>2</sub>O<sub>3</sub> nanotube arrays and bare CC/TiO<sub>2</sub> nanotube arrays increased marginally, while that of the CC/Fe<sub>2</sub>O<sub>3</sub> composites increased significantly.

## CONCLUSIONS

3D hierarchical charantia-like TiO<sub>2</sub>/Fe<sub>2</sub>O<sub>3</sub> nanotube arrays were fabricated on CC by a simple, two-step, seed-free hydrothermal method. The well-wrapped mesoporous Fe<sub>2</sub>O<sub>3</sub> nanospheres on TiO<sub>2</sub> nanotubes endowed the final nanotube arrays with a larger specific surface area. The hollow framework and its direct contact with the CC current collector led to the good conductivity of the electrode. The low volume expansion of the hollow TiO<sub>2</sub> cores combined with the strong adhesion between the two types of metal oxides stabilized the structure of the final nanotube arrays during cycling. The electrochemical results revealed that the charantia-like TiO<sub>2</sub>/Fe<sub>2</sub>O<sub>3</sub> nanotube arrays have high reversible capacity, improved cycling stability, and excellent rate capability. After 200 cycles at a current density of 200 mA g<sup>-1</sup>, the capacity of the nanotube arrays remained at 875 mAh g<sup>-1</sup>. A rate capability of ~742 mAh g<sup>-1</sup> was achieved even when the discharge rate was increased to 1,600 mA g<sup>-1</sup>.

## DATA AVAILABILITY STATEMENT

The datasets generated for this study are available on request to the corresponding author.

## AUTHOR CONTRIBUTIONS

PX, HZ, AS, and YZha conducted the synthesis. PX, YZha, and YW carried out the characterization and the electrochemical measurements. PX and ZZ co-wrote the manuscript. All authors discussed the data and commented on the manuscript.

## REFERENCES

- Deng, S., Zhang, Y., Xie, D., Yang, L., Wang, G., Zheng, X. S., et al. (2019). Oxygen vacancy modulated  $\text{Ti}_2\text{Nb}_{10}\text{O}_{29-x}$  embedded onto porous bacterial cellulose carbon for highly efficient lithium ion storage. *Nano Energy* 58, 355–364. doi: 10.1016/j.nanoen.2019.01.051
- Gao, G., Yu, L., Wu, H. B., and Lou, X. W. (2014). Hierarchical tubular structures constructed by carbon-coated  $\alpha\text{-Fe}_2\text{O}_3$  nanorods for highly reversible lithium storage. *Small* 10, 1741–1745. doi: 10.1002/sml.201303818
- Han, H., Song, T., Bae, Y. J., Nazar, L. F., Kim, H., and Paik, U. (2011). Nitridated  $\text{TiO}_2$  hollow nanofibers as an anode material for high power lithium ion batteries. *Energy Environ. Sci.* 4, 4532–4536. doi: 10.1039/c1ee02333k
- He, J., Chen, Y., and Manthiram, A. (2018). Vertical  $\text{Co}_9\text{S}_8$  hollow nanowall arrays grown on a Celgard separator as a multifunctional polysulfide barrier for high-performance Li-S batteries. *Energy Environ. Sci.* 67611, 2560–2568. doi: 10.1039/C8EE00893K
- Jiang, T., Bu, F., Feng, X., Shakir, I., Hao, G., and Xu, Y. (2017). Porous  $\text{Fe}_2\text{O}_3$  nanoframeworks encapsulated within three-dimensional graphene as high-performance flexible anode for lithium-ion battery. *ACS Nano* 11, 5140–5147. doi: 10.1021/acsnano.7b02198
- Joshi, B. N., An, S., Jo, H. S., Song, K. Y., Park, H. G., Hwang, S., et al. (2016). Flexible, freestanding, and binder-free  $\text{SnOx-ZnO}$ /carbon nanofiber composites for lithium ion battery anodes. *ACS Appl. Mater. Interfaces* 8, 9446–9453. doi: 10.1021/acsmi.6b01093
- Larcher, D., Bonnin, D., Cortes, R., Rivals, I., Personnaz, L., and Tarascon, J. M. (2003). Combined XRD, EXAFS, and mossbauer studies of the reduction by lithium of  $\alpha\text{-Fe}_2\text{O}_3$  with various particle size. *J. Electrochem. Soc.* 150, A1643–A1650. doi: 10.1149/1.1622959
- Lee, G., Kim, S., Kim, S., and Choi, J. (2017).  $\text{SiO}_2/\text{TiO}_2$  composite film for high capacity and excellent cycling stability in lithium-ion battery anodes. *Adv. Funct. Mater.* 27:1703538. doi: 10.1002/adfm.201703538
- Li, Y. Y., Cai, Q. F., Wang, L., Li, Q. W., Peng, X., Gao, B., et al. (2016). Mesoporous  $\text{TiO}_2$  nanocrystals/graphene as an efficient sulfur host material for high-performance lithium-sulfur batteries. *ACS Appl. Mater. Interfaces* 8, 23784–23792. doi: 10.1021/acsmi.6b09479
- Liu, B., Zhang, Y., Pan, G., Ai, C., Deng, S., Liu, S., et al. (2019). Ordered lithiophilic sites to regulate Li plating/stripping behavior for superior lithium metal anodes. *J. Mater. Chem. A* 7, 21794–21801. doi: 10.1039/C9TA09502K
- Luo, J. S., Xia, X. H., Luo, Y. S., Guan, C., Liu, J. L., Qi, X. Y., et al. (2013). Rationally designed hierarchical  $\text{TiO}_2/\text{Fe}_2\text{O}_3$  hollow nanostructures for improved lithium ion storage. *Adv. Energy Mater.* 3, 737–743. doi: 10.1002/aenm.201200953
- Luo, Y., Luo, J., Jiang, J., and Zhou, W. (2012). Seed-assisted synthesis of highly ordered  $\text{TiO}_2/\alpha\text{-Fe}_2\text{O}_3$  core/shell arrays on carbon textiles for lithium-ion battery applications. *Energy Environ. Sci.* 5, 6559–6566. doi: 10.1039/c2ee03396h
- Moretti, A., Kim, G. T., Bresser, D., Renger, K., Paillard, E., Marassi, R., et al. (2013). Investigation of different binding agents for nanocrystalline anatase  $\text{TiO}_2$  anodes and its application in a novel, green lithium-ion battery. *J. Power Sources* 221, 419–426. doi: 10.1016/j.jpowsour.2012.07.142

## FUNDING

This work was supported by National Natural Science Foundation of China (grant no. 71401106), Natural Science Foundation of Shanghai (grant no. 14ZR1418700), and Shanghai University of Engineering Science Innovation Fund (grant no. 18KY0504).

## ACKNOWLEDGMENTS

The authors would like to thank Minjie Yan for his help with SEM/EDX analysis.

- Partheeban, T., and Sasidharan, M. (2019). Template-free synthesis of  $\text{LiV}_3\text{O}_8$  hollow microspheres as positive electrode for Li-ion batteries. *J. Mater. Sci.* 55, 2155–2165. doi: 10.1007/s10853-019-04086-3
- Qi, X., Zhang, H., Zhang, Z., Bian, Y., Shen, A., Xu, P., et al. (2018). Subunits controlled synthesis of three-dimensional hierarchical flower-like  $\alpha\text{-Fe}_2\text{O}_3$  hollow spheres as high-performance anodes for lithium ion batteries. *Appl. Surf. Sci.* 452, 174–180. doi: 10.1016/j.apsusc.2018.04.253
- Shen, S., Guo, W., Xie, D., Wang, Y., Deng, S., Zhong, Y., et al. (2018). A synergistic vertical graphene skeleton and S-C shell to construct high-performance  $\text{TiNb}_2\text{O}_7$ -based core/shell arrays. *J. Mater. Chem. A* 6, 20195–20204. doi: 10.1039/C8TA06858E
- Shen, S., Xia, X., Zhong, Y., Deng, S., Xie, D., Liu, B., et al. (2019). Implanting niobium carbide into trichoderma spore carbon: a new advanced host for sulfur cathodes. *Adv. Mater.* 31:1900009. doi: 10.1002/adma.201900009
- Smith, K. A., Savva, A. I., Mao, K. S., Wang, Y., Tenne, D. A., Chen, D., et al. (2019). Effect of proton irradiation on anatase  $\text{TiO}_2$  nanotube anodes for lithium-ion batteries. *J. Mater. Sci.* 54, 13221–13235. doi: 10.1007/s10853-019-03825-w
- Wang, C., Wu, L., Wang, H., Zuo, W., Li, Y., and Liu, J. (2015). Fabrication and shell optimization of synergistic  $\text{TiO}_2\text{-MoO}_3$  core-shell nanowire array anode for high energy and power density lithium-ion batteries. *Adv. Funct. Mater.* 25, 3524–3533. doi: 10.1002/adfm.201500634
- Wang, X., Fan, L., Gong, D., Zhu, J., Zhang, Q., and Lu, B. (2016). Core-shell  $\text{Ge@Graphene@TiO}_2$  nanofibers as a high-capacity and cycle-stable anode for lithium and sodium ion battery. *Adv. Funct. Mater.* 26, 1104–1111. doi: 10.1002/adfm.201504589
- Wang, Z., Luan, D., Madhavi, S., Hu, Y., and Lou, X. (2012). Assembling carbon-coated  $\alpha\text{-Fe}_2\text{O}_3$  hollow nanohorns on the CNT backbone for superior lithium storage capability. *Energy Environ. Sci.* 5, 5252–5256. doi: 10.1039/C1EE02831F
- Xia, H., Xiong, W., Lim, C. K., Yao, Q. F., Wang, Y. D., and Xie, J. P. (2014). Hierarchical  $\text{TiO}_2\text{-B}$  nanowire@ $\alpha\text{-Fe}_2\text{O}_3$  nanothorn core-branch arrays as superior electrodes for lithium ion microbatteries. *Nano Res.* 7, 1797–1808. doi: 10.1007/s12274-014-0539-3
- Yang, J., Wu, Q., Yang, X., He, S., Khan, J., Meng, Y., et al. (2017). Chestnut-like  $\text{TiO}_2/\alpha\text{-Fe}_2\text{O}_3$  core-shell nanostructures with abundant interfaces for efficient and ultralong life lithium-ion storage. *ACS Appl. Mater. Inter.* 9, 354–361. doi: 10.1021/acsmi.6b12150
- Yang, Y., Wang, S., Lin, S., Li, Y., Zhang, W., Chao, Y., et al. (2018). Rational design of hierarchical  $\text{TiO}_2$ /epitaxially aligned  $\text{MoS}_2$ -carbon coupled interface nanosheets core/shell architecture for ultrastable sodium-ion and lithium-sulfur batteries. *Small Methods* 2:1800119. doi: 10.1002/smt.201800119
- Ying, W., Yu, J., Shi, J., Gu, L., and Yu, Y. (2017). Multichannel porous  $\text{TiO}_2$  hollow nanofibers with rich oxygen vacancies and high grain boundary density enabling superior sodium storage performance. *Small* 13:1700129. doi: 10.1002/sml.201700129
- Zhang, Z., Xu, P., Zhang, H., Shen, A., and Zhao, Y. (2019). Flexible three-dimensional titanium-dioxide-based hollow nanoflower arrays for advanced lithium-ion battery anodes. *ACS Appl. Energy Mater.* 2, 5744–5752. doi: 10.1021/acsaem.9b00869

- Zhao, Q., Liu, J., Li, X., Xia, Z., Zhang, Q., Zhou, M., et al. (2019). Graphene oxide-induced synthesis of button-shaped amorphous  $\text{Fe}_2\text{O}_3/\text{rGO}/\text{CNFs}$  films as flexible anode for high-performance lithium-ion batteries. *Chem. Eng. J.* 369, 215–222. doi: 10.1016/j.cej.2019.03.076
- Zhao, Y., Li, X., Yan, B., Xiong, D., Li, D., Lawes, S., et al. (2016). Recent developments and understanding of novel mixed transition-metal oxides as anodes in lithium ion batteries. *Adv. Energy Mater.* 6:1502175. doi: 10.1002/aenm.201502175
- Zhu, C., Xia, X., Liu, J., and Fan, Z., (2014).  $\text{TiO}_2$  nanotube@ $\text{SnO}_2$  nanoflake core-branch arrays for lithium-ion battery anode. *Nano Energy* 4, 105–112. doi: 10.1016/j.nanoen.2013.12.018

**Conflict of Interest:** The authors declare that the research was conducted in the absence of any commercial or financial relationships that could be construed as a potential conflict of interest.

Copyright © 2020 Xu, Zhang, Zhang, Shen, Zhao, Zhou and Weng. This is an open-access article distributed under the terms of the Creative Commons Attribution License (CC BY). The use, distribution or reproduction in other forums is permitted, provided the original author(s) and the copyright owner(s) are credited and that the original publication in this journal is cited, in accordance with accepted academic practice. No use, distribution or reproduction is permitted which does not comply with these terms.